Received: 28 March 2022 | Revised: 28 April 2022 | Accepted: 6 May 2022

DOI: 10.1002/cey2.233

RESEARCH ARTICLE

CARBON ENERGY WILEY

Sulfur and nitrogen codoped cyanoethyl cellulose-derived carbon with superior gravimetric and volumetric capacity for potassium ion storage

Guangzeng Cheng[1] | Wenzhe Zhang[1] | Wei Wang[1] | Huanlei Wang[1] | Yixian Wang[2] | Jing Shi[1] | Jingwei Chen[1] | Shuai Liu[1] | Minghua Huang[1] | David Mitlin[2]

[1]School of Materials Science and Engineering, Ocean University of China, Qingdao, Shandong, China

[2]Materials Science and Engineering Program, Texas Materials Institute (TMI), The University of Texas at Austin, Austin, Texas, USA

Correspondence
Huanlei Wang, School of Materials Science and Engineering, Ocean University of China, Qingdao 266100, China.
Email: huanleiwang@gmail.com and huanleiwang@ouc.edu.cn

David Mitlin, Materials Science and Engineering Program, Texas Materials Institute, The University of Texas at Austin, Austin, TX 78712-159, USA.
Email: david.mitlin2@utexas.edu

Funding information
National Natural Science Foundation of China, Grant/Award Numbers: 22179123, 21471139; Natural Science Foundation of Shandong Province, Grant/Award Number: ZR2020ME038; Fundamental Research Funds for the Central Universities, Grant/Award Number: 201941010; National Science Foundation, Division of Materials Research, Grant/Award Number: 1938833

Abstract

We fabricated sulfur and nitrogen codoped cyanoethyl cellulose-derived carbons (SNCCs) with state-of-the-art electrochemical performance for potassium ion battery (PIB) and potassium ion capacitor (PIC) anodes. At 0.2, 0.5, 1, 2, 5, and 10 A g^{-1}, the SNCC shows reversible capacities of 369, 328, 249, 208, 150, and 121 mA h g^{-1}, respectively. Due to a high packing density of 1.01 g cm^{-3}, the volumetric capacities are also uniquely favorable, being 373, 331, 251, 210, 151, and 122 mA h cm^{-3} at these currents, respectively. SNCC also shows promising initial Coulombic efficiency of 69.0% and extended cycling stability with 99.8% capacity retention after 1000 cycles. As proof of principle, an SNCC-based PIC is fabricated and tested, achieving 94.3 Wh kg^{-1} at 237.5 W kg^{-1} and sustaining over 6000 cycles at 30 A g^{-1} with 84.5% retention. The internal structure of S and N codoped SNCC is based on highly dilated and defective graphene sheets arranged into nanometer-scale walls. Using a baseline S-free carbon for comparison (termed NCC), the role of S doping and the resultant dilated structure was elucidated. According to galvanostatic intermittent titration technique and electrochemical impedance spectroscopy analyses, as well as COMSOL simulations, this structure promotes rapid solid-state diffusion of potassium ions and a solid electrolyte interphase that is stable during cycling. X-ray diffraction was used to probe the ion storage mechanisms in SNCC, establishing the role of reversible potassium intercalation and the presence of KC_{36}, KC_{24}, and KC_8 phases at low voltages.

KEYWORDS
carbon manufacturing; commercial carbon; graphene; potassium ion battery (KIP, PIB); potassium ion storage

1 | INTRODUCTION

Lithium-ion batteries (LIBs) dominate as the main power sources for electric vehicles and electronic equipment, with increasing demand in the foreseeable future.[1–5] However, due to the scarcity of lithium resources, there is a need to develop alternative ion chemistries that will complement LIBs in lower-cost applications such as stationary energy storage and backup power.[6–10] Potassium-ion batteries (PIBs) have received extensive attention due to the geographic abundance and the low price of potassium precursors as well as the K/K^+ redox potential that is on par with that of Li/Li^+.[11–22] Graphite may be used as a PIB anode to form a terminal KC_8 intercalation compound with a theoretical specific capacity of 279 mA h g^{-1}.[22] The first electrochemical intercalation of K into graphite at room temperature was investigated by Ji et al.'s[16] group, in which commercial synthetic graphite was used in a K/graphite half-cell to produce a capacity of 273 mA h g^{-1} at the C/40. The K/graphite cell was also tested for high-current rate-cycling producing capacities of 263 and 80 mA h g^{-1} at C/10 and 1C, respectively. Thus, while graphite can show a large capacity at low current rates, its capacity drops dramatically upon application of higher current rates.[16] The application of graphite anodes in PIBs is limited by the large volume expansion of the lattice associated with the intercalation, leading to cycling-induced exfoliation of the anodes.[19,20] Design of new potassium-specific electrolyte systems is a key promising approach for enhancing the cycling stability of PIBs. This approach includes creating potassium-specific concentrated electrolyte systems.[21,22] For example, Lu et al.'s[22] group used a concentrated KFSI electrolyte to induce the formation of a robust inorganic-rich passivation layer on the graphite anode, realizing stable cycling performance with up to 2000 cycles. The same group created an aqueous electrolyte based on $Fe(CF_3SO_3)_3$ modified 21 M KCF_3SO_3 to enhance the structural and surface chemical stability of the electrode and achieve an impressive lifetime of 130,000 cycles (more than 500 days).[21]

Researchers have also focused on nongraphitic carbons with defective and dilated graphene layers as candidates for fast charge-extended cycling PIB anodes.[3,23,24] For example, Pint et al.'s[23] group demonstrated that N doping of the graphitic carbon could considerably increase the K-storage capacity in graphite. Our group reported the synthesis of sulfur-rich graphene nanoboxes, in which sulfur can conjugate with the graphene layer and expand the layer spacing, achieving 516 mA h g^{-1} at 50 mA g^{-1} and a reversible capacity of 172 mA h g^{-1}after 1000 cycles at 2000 mA g^{-1}.[25] Moreover, our group also prepared a S-doped N-rich carbon, which achieves a high capacity of 437 mA h g^{-1} at 100 mA g^{-1} and 234 mA h g^{-1} at 1000 mA g^{-1}.[24] A surface-driven capacitive mechanism is widely reported in porous carbons, hard carbons, soft carbons, and their composites.[26–36] These carbon materials usually have high specific surface areas with defective structures, which shortens the ion transport length and provides a large electrode/electrolyte interface for charge storage, leading to enhanced specific capacity and rate capability.[30,37–45] However, these high-surface-area carbons usually show relatively low initial Coulombic efficiencies (ICEs).[46] To alleviate this problem, authors reported a structurally and chemically defective activated–crumbled graphene as PIB anodes, showing a specific capacity of 340 mA h g^{-1} at 40 mA g^{-1} and an ICE of 41%.[47] Precursors for nongraphitic carbons can be cellulose and its derivates, being inexpensive and scalable, with a wide range of structures being achieved through refinement of the pyrolysis conditions.[48–57] In the 1950s, cyanoethyl cellulose (CEC) was prepared by direct cyanoethylation of cotton and commercialized.[58] CEC has applications in numerous fields like electroluminescent materials, emulsifiers, nonionic surfactants, new radar screens, large-screen television transmission screens, and small capacitors for lasers.[59]

Most studies focus on increasing the gravimetric capacity, while the volumetric capacity of the electrode has been less widely reported.[60] Since many energy storage systems are designed based on the available volume, an improvement of volumetric performance is desirable.[61] In this regard, several strategies, including high-temperature carbonization of biomass, creating a optimally packed microtopography, and a sulfur-assisted synthesis strategy, have been proposed to increase the volumetric capacity of energy storage devices.[61–63] For example, authors reported dense hard carbon derived from leftover silkworm feed, showing a low specific surface area.[61] Han et al.'s[62] group developed a graphene assembly with a controllable pore structure using sulfur as a template. When used as the anode material for PIBs, this carbon assembly yielded a high volumetric capacity (144 mA h cm^{-3}) after 500 cycles. Zhang et al.'s[63] group reported a nitrogen/oxygen codoped carbon hollow multihole bowl-based electrode, which has a 56% higher volumetric capacity than that of hollow spheres due to the tap density of the bowl-shaped particles. In general, it is desirable to design anode materials for potassium ion batteries with improved volumetric capacity and ICE.

Herein, we use CEC as the precursor to prepare a dense, low-surface-area N, S codoped carbon (sulfur and nitrogen codoped cyanoethyl cellulose-derived carbon [SNCC]) by mimicking the commercial procedure for the fabrication of viscose. Viscose is an inexpensive and

versatile fabric that is commonly used as a substitute for silk.[64,65] It is produced when cellulose raw materials are treated with sodium hydroxide and carbon disulfide to obtain orange cellulose sodium xanthate, which is dissolved in a dilute sodium hydroxide solution to yield a viscous spinning stock solution.[66,67] The SNCC internal structure promotes facile diffusion of potassium ions, thus obtaining excellent rate capacity, but without sacrificing the ICE. A broad comparison with the literature on carbon anodes for potassium indicates that the achieved combination of gravimetric and volumetric electrochemical performance is among the most competitive.

2 | EXPERIMENTAL

2.1 | Synthesis of S, N codoped CEC-derived carbon

As a starting point, 3 g of CEC was added in a 20 wt% NaOH solution (60 mL) under stirring for 1 h. Then, 3 mL of CS_2 was added dropwise to the above suspension and stirred for another 4 h, followed by a 5 wt% $MgSO_4$ solution (100 mL) that was subsequently added to the solution and stirred for 15 min. Then, 300 mL of ethyl alcohol was added to the solution and stirred for 8 h. After collecting the precursors by filtration and washing, the obtained powder was carbonized at 800°C for 3 h at a heating rate of 3°C min^{-1} under a N_2 atmosphere. Finally, the SNCC powder was obtained by washing with 2 M HCl and deionized water, followed by drying at 80°C for 12 h in a vacuum. As an additional baseline, N-doped cyanoethyl cellulose-derived carbon (NCC) was obtained by the direct carbonization of CEC.

2.2 | Materials characterization

The morphology, structure, and chemical content of the carbons were characterized by scanning electron microscopy (SEM; Hitachi S4800) and transmission electron microscopy (TEM; JEOL 2010F). X-ray diffraction (XRD) measurements were conducted using a Bruker D8 advance diffractometer using Cu-Kα radiation. Raman tests were carried out at a Lab RAM HR800 with a 532-nm excitation wavelength laser. The electron spin resonance (ESR; Bruker EMXnano) was performed to test the content of unpaired electrons in the samples. The specific surface areas and pore size distributions of the samples were characterized at 77 K on a Belsorp Max surface area and pore analyzer. X-ray photoelectron spectroscopy (XPS) measurements were performed using a Thermo Scientific ESCALAB 250XI to determine the chemical composition. For post-mortem XRD analysis, electrodes at different potassiation/depotassiation stages were disassembled in an argon-filled glovebox and then washed using 1,2-dimethoxyethane (DME). The packing density of the electrode was measured using a cylindrical rod to press the sample into a mold at a pressure of 10 MPa, and the measurements were repeated three times with an error smaller than 3%.

2.3 | Electrochemical measurements

A slurry was formed by mixing the active materials, carboxymethylcellulose, and Super P in a mass ratio of 75:15:10 in a water/ethanol solvent. This slurry was pasted onto a Cu foil and dried for 12 h at 80°C to obtain the working electrode. The average mass loading of the active materials was around 0.8 mg cm^{-2}. CR2032-type cells were assembled using potassium metal as a counter electrode and a Whatman glass microfiber filter as a separator in an argon-filled glovebox (O_2 and $H_2O < 0.1$ ppm). The electrolyte was potassium bis (fluorosulfonyl)imide (KFSI), DME, and 1,1,2,2-tetrafluoroethyl-2,2,2-trifluoroethyl ether mixed in a molar ratio of 1:1.90:0.95. Galvanostatic potassiation/depotassiation tests and galvanostatic intermittent titration technique (GITT) analysis were performed using a Land CT2001A battery testing system. Cyclic voltammetry (CV) curves and electrochemical impedance spectroscopy (EIS) were recorded on a CHI660E electrochemical workstation.

Potassium ion capacitors (PICs) were assembled using SNCC as the anode and the N, S codoped porous carbon (NS-PC) reported in the previous literature as the cathode. The preparation process of NS-PC PIC cathode material is as follows: methylcellulose (2.0 g) was thoroughly mixed with thiourea (2.0 g) and $NaHCO_3$ (10.0 g) in an agate mortar. The obtained mixture was precarbonized at 200°C for 2 h and then carbonized at 700°C for 4 h, both in an inert N_2 environment. The final NS-PC material was obtained after washing and drying. More details of the synthesis process are provided by Piao et al.[68] Both the SNCC anode and the NS-PC cathode were activated in a half-cell at 0.1 A g^{-1} for three cycles and terminated at a voltage of 1.5 V. After activation, the SNCC anode was assembled with the NS-PC cathode to form PICs. The electrochemical performances of PICs with different anode-to-cathode mass ratios were determined in a working voltage window of 0–3.8 V. The PIC specific energy (E, Wh kg^{-1}) and specific power (P, W kg^{-1}) are calculated based on the following relations:

$$\Delta V = 0.5(V_{max} + V_{min}),$$

$$P = \Delta V \times i/m,$$

$$E = P \times t,$$

where V_{max} is the initial discharge voltage excluding IR drop, V_{min} is the voltage at the end of discharge, i is the discharge current, m is the combined active mass of the anode and the cathode, and t is the discharge time. It should be pointed out that while the current density for both half-cells and full devices is based on the active mass of the anode, the device energy and power are calculated based on the active mass in both electrodes.

2.4 | COMSOL Multiphysics calculation

The finite element method (FEM) was used to investigate the distribution of K^+ through the NCC (0.349 nm) and SNCC (0.363 nm) by COMSOL Multiphysics. Two physical models of electrostatic and transport of diluted species based on the Nernst–Plank Equation ($N_K = -D_K\nabla = c_K(1 - u_K\nabla\ \varphi)$, $\partial c/\partial t = -\nabla N_K$) were coupled to conduct FEM simulations. N_K is the flux vector of K^+, D_K is the diffusion coefficient of K^+, c_K is the concentration of K^+, φ is the electric potential, u_K is the ionic mobility of K^+ in electrolytes, and t is the diffusion time. The geometrical size of FEM simulation was set as $20 \times 10\ \mu m$ in a rectangular area. These FEM simulations were performed separately for our conventional composite separators (electrolyte and electrode) in the rectangular area. To investigate ion transport behavior with limited volume of liquid electrolyte, the same physical model was used. Moreover, the ratio of the diffusion coefficient of K ions in the liquid electrolyte and in solid particles was set to eight according to studies of Zhao et al.[69] and Deng et al.[70] The mobilities of K^+ ions in the liquid electrolyte and in the solid particles were calculated by FEM to solve the Nernst–Plank equation.

3 | RESULTS AND DISCUSSION

Figure 1 shows the synthesis diagram of SNCC, where a CEC precursor is first synthesized analogously for the fabrication of viscose and then carbonized under an inert atmosphere. Alkalized CEC is obtained through the reaction of N–cell–OH + NaOH → N–cell–ONa. The purpose of the alkalization process is to obtain an alkaline environment for improving the activity of the following reaction between –ONa and CS_2. By the addition of CS_2, the alkalized CEC is reacted with CS_2 to form CEC xanthate sodium, the reaction being N–cell–ONa + CS_2 → N–cell–OCS_2Na. This step improves the solubility of precursors in an alkali solution.[71] The introduction of sulfur species into the precursor also results in more potassium ion-active structural and chemical defect sites post carbonization. Afterward, CEC xanthate sodium is immersed in the $MgSO_4$ solution, with the aim of replacing Na^+ with Mg^{2+} by ion exchange: 2N–cell–OCS_2Na + Mg^{2+} → $(N–cell–OCS_2)_2Mg$. It is known that ion exchange with Mg^{2+} can make the resulting precursor more stable.[49] Finally, CEC xanthate magnesium is carbonized to obtain SNCC, during which Mg^{2+} is converted into MgO (Figure S1), playing the role of a sacrificial template that results in internal graphene array "walls" that are nanometer scale, in turn reducing the solid-state diffusion distances. However, the resultant increase in the surface area is relatively modest, reducing the extent of parasitic reactions of the carbon with the electrolyte at cycle one. The MgO is removed by the subsequent washing step. In principle, by mimicking the synthesis method for commercial viscose while including a straightforward carbonization step that does not use chemical activation agents such as KOH, the dual-doped carbon can be mass produced.

Figure 2 shows the morphology and structure of SNCC and NCC. As indicated by the SEM images in Figures 2A and S2A, SNCC has a honeycomb-like surface topography. This can be attributed to the fact that the magnesium ions in the chains of modified CEC transform into MgO during the carbonization, the final

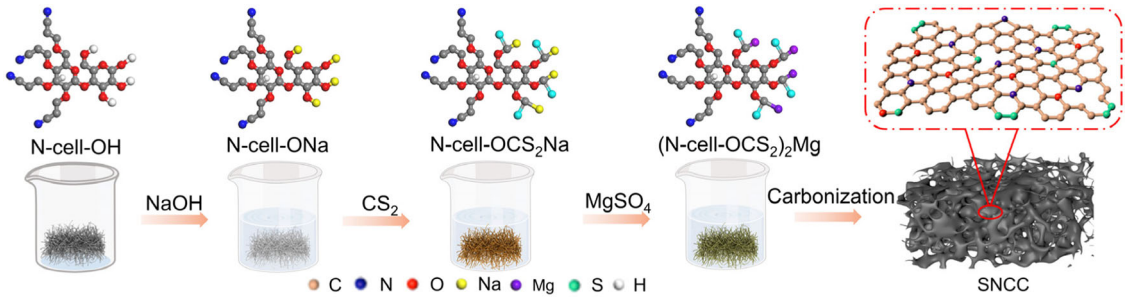

FIGURE 1 Schematic illustration for the synthesis process used to fabricate SNCC, detailing the key steps and the resultant structure. SNCC, S, N codoped cyanoethyl cellulose-derived carbon.

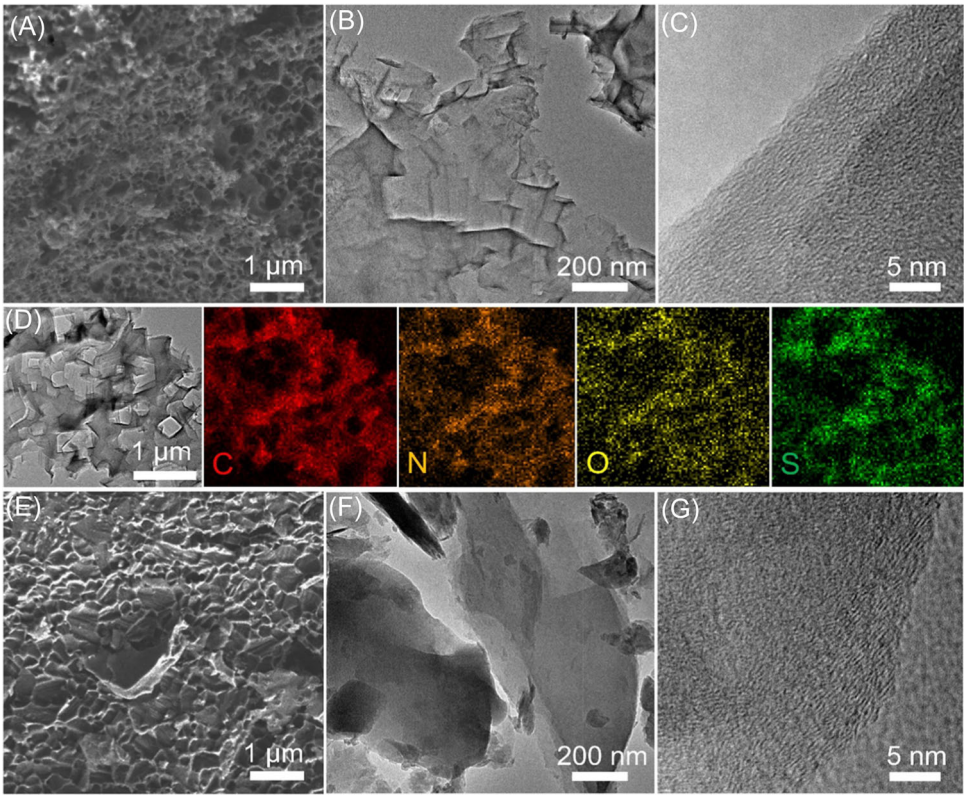

FIGURE 2 (A) SEM image for SNCC, (B) TEM image of SNCC, and (C) high-resolution TEM image of SNCC. (D) HAADF-TEM image and the corresponding EDXS elemental distributions of C, N, O, and S in SNCC. (E) SEM image for baseline NCC, (F) TEM image of NCC, and (G) high-resolution TEM image of NCC. EDXS, energy-dispersive X-ray spectroscopy; ENCC, N-doped cyanoethyl cellulose-derived carbon; HAADF, high-angle annular dark-field; SEM, scanning electron microscopy; SNCC, S, N codoped cyanoethyl cellulose-derived carbon; TEM, transmission electron microscopy.

shape being obtained after the removal of MgO. TEM analysis of the SNCC structure is presented in Figure 2B,C. It may be observed that SNCC is composed of aggregates of nanometer-scale (according to the mass-thickness contrast) walls of highly defective graphene. As expected, there is no evidence of well-defined graphitization in the material. Figure 2D shows a TEM-obtained energy-dispersive X-ray spectroscopy elemental map of SNCC, highlighting the uniform (within resolution limit) distribution of C, N, O, and S throughout the carbon. Figures 2E and S2B show the analogous SEM and TEM analyses of baseline NCC, highlighting its blockier morphology both at the macroscale and at the microscale. According to Figure 2F,G the stronger mass-thickness contrast present with NCC indicates thicker carbon walls as compared to SNCC.

The crystal structures of NCC and SNCC were further analyzed by XRD and Raman analyses. Figure 3A compares the XRD patterns of NCC and SNCC. The SNCC and NCC carbons possess a single peak centered at 24.5° and 25.5°, respectively. This agrees with previous reports for nongraphitic carbons, for example, Chen et al.,[42] with the peak center corresponding to the mean spacing of the highly defective (002) planes. According to Bragg's law, this mean layer spacings for SNCC and NCC are 0.363 and 0.349 nm, respectively, demonstrating the role of sulfur doping in increasing the mean distance. To further determine the difference between the structures of the two carbons, an empirical parameter R was used. Basically, a higher R value is indicative of less randomly stacked graphene layers and a higher degree of order.[72] The method for R calculation and the corresponding values are shown in Figure S3 and Table S1. The R value of SNCC is 1.42 versus 2.42 for that of NCC, highlighting differences in their structure. The Raman analysis shown in Figure 3B demonstrates that SNCC and NCC have two representative peaks at 1330 (D band) and 1590 cm^{-1} (G band), corresponding to the disordered structure and the graphitic sp^2 carbon structure, respectively.[73–75] In addition, the T band at 1180 cm^{-1} is attributed to the presence of O/S heteroatoms or impurities, and the D′′ band at 1498 cm^{-1} corresponds to amorphous carbon.[56,76] The intensity ratio of the D and G bands (I_D/I_G) can be used to assess the degree of disorder of the two samples. SNCC shows an I_D/I_G ratio of 1.64, while NCC has a ratio of 1.46, in agreement with the XRD results.

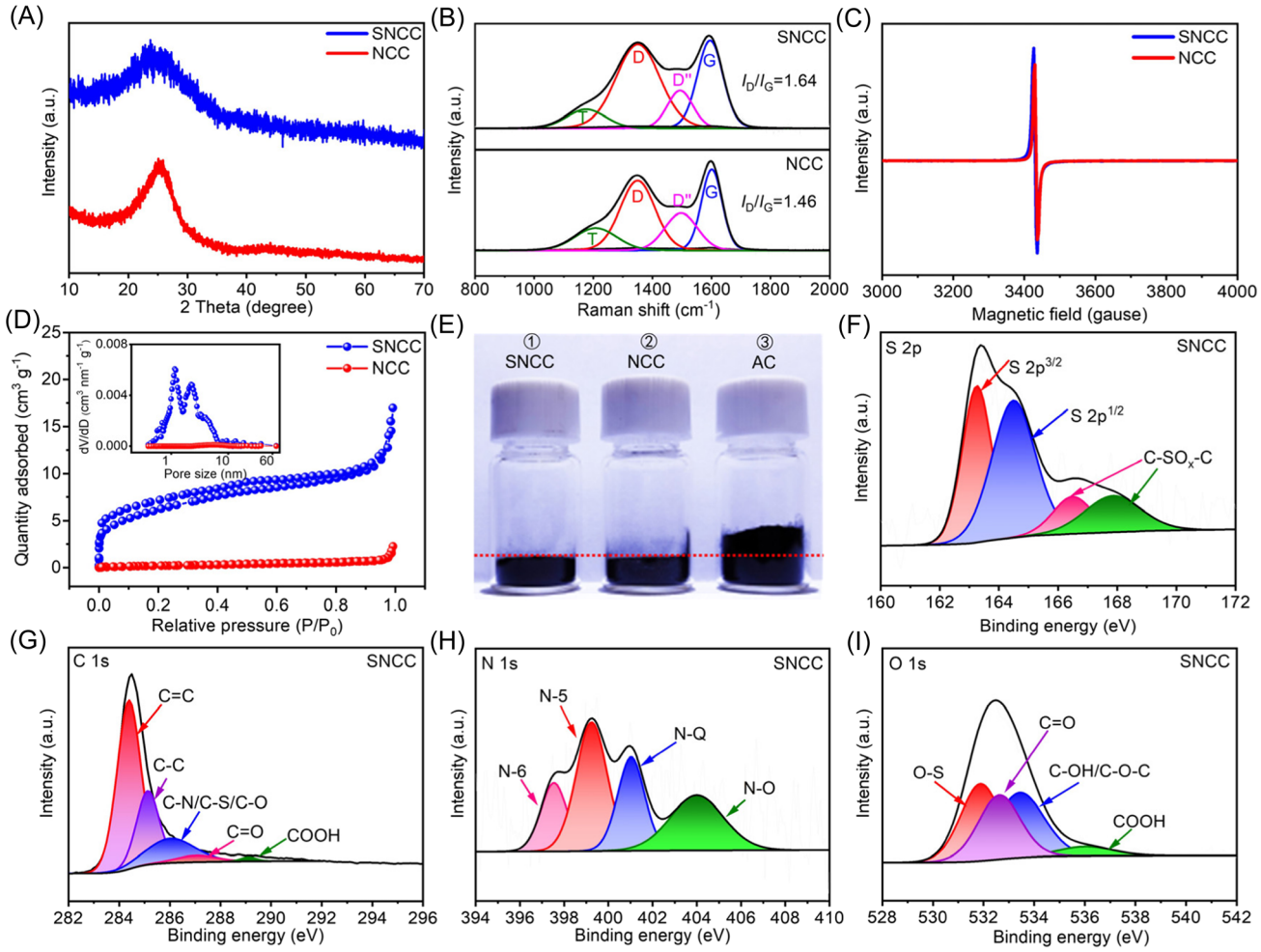

FIGURE 3 (A) XRD spectra of SNCC and NCC showing a single highly broadened diffraction peak, centered at $2\theta = 24.5°$ and 25.5°, respectively. (B) Raman spectra of SNCC and NCC. (C) ESR spectra of SNCC and NCC. (D) Nitrogen adsorption–desorption isotherms of SNCC and NCC, with the inset showing the pore size distribution based on DFT. (E) Digital photographs of SNCC, NCC, and commercial AC. High-resolution XPS spectra of SNCC: (F) S 2p, (G) C 1s, (H) N 1s, and (I) O 1s. AC, activated carbon; DFT, density functional theory; ESR, electron spin resonance; NCC, N-doped cyanoethyl cellulose-derived carbon; SNCC, S, N codoped cyanoethyl cellulose-derived carbon; XPS, X-ray photoelectron spectroscopy; XRD, X-ray diffraction.

Figure 3C shows the ESR spectra for SNCC and NCC. The peak located at a magnetic field of ca. 3430 Gauss with the corresponding g values of 2.0014 and 2.0009 is ascribed to the free electrons.[77] The enhanced peak intensity with SNCC indicates the increased density of unpaired electrons that originate from defects in the carbon, consistent with XRD and Raman results.

Figure 3D shows the nitrogen absorption–desorption isothermal curves of SNCC and NCC, and both SNCC and NCC show type IV isotherms. The Brunauer–Emmett–Teller (BET) specific surface area of NCC is 1 $m^2 g^{-1}$. Due to the sacrificial template effect of the MgO, the surface area of SNCC is 22 $m^2 g^{-1}$, still modest, albeit an order of magnitude higher than the baseline. The pore volume of SNCC is 0.028 $cm^3 g^{-1}$, versus 0.003 $cm^3 g^{-1}$ for that of NCC. The surface area of SNCC is comparable to that of the reported hard carbons (usually <100 $m^2 g^{-1}$),[78,79] but significantly smaller than that for porous carbons (500–2000 $m^2 g^{-1}$).[80–82] The low-surface area of SNCC ensures a favorable density for the pressed electrodes. The pore size distribution indicates that SNCC has more macro/mesopores as compared to NCC, which is beneficial for the potassium ion transport in the electrolyte. The increased porosity can also provide more buffer space for accommodating the internal stresses, although the thinner internal wall thickness in SNCC (according to TEM result) likely is more important for that effect. The difference between the density of SNCC, NCC, and conventional activated carbon can be seen more intuitively in Figure 3E. The measured packing densities of SNCC and NCC are 1.01 and 1.07 g cm^{-3}, respectively, being twice that of AC at 0.53 g cm^{-3}.

The composition and bonding of SNCC and NCC were analyzed by XPS. According to the survey spectra in Figure S4, SNCC shows peaks corresponding to C 1s, N 1s, O 1s, S 2p, and S 2s, while NCC only shows peaks of C 1s, N 1s, and O 1s. According to Table S1, the sulfur content in SNCC is 1.42 wt%. The S 2p spectrum can be divided into four peaks (Figure 3F), located at 163.3, 164.5, 166.5, and 167.9 eV. The first two peaks correspond to S $2p^{3/2}$ and S $2p^{1/2}$ of the C–S/S–S covalent bond due to the spin–orbital splitting of the element S, while the other two peaks are related to sulfur oxide.[24,83] The C–S/S–S bonded sulfur have been shown to participate in the reversible redox reactions with K^+, providing additional capacity.[84] As shown in Table S2, the proportion of C–S/S–S bonds is up to 75.13%. According to Figures 3G and S5A, the high-resolution XPS C 1s spectra for SNCC and NCC can be decomposed into five peaks, located at 284.4, 285.1, 285.9, 286.9, and 289.2 eV. These represent the C═C, C–C, C–N/C–S/C–O, C═O, and COOH functional groups, respectively.[85] It can be observed that the sp^2 C═C content decreases from 59.91% in NCC to 53.72% in SNCC, while the sp^3 C–C content increases from 19.72% in NCC to 22.61% in SNCC (Table S3). This further supports the fact that sulfur doping promotes the formation of defects.

Figures 3H and S5B show the high-resolution XPS N 1s spectra for SNCC and NCC, respectively. The spectra consist of four peaks: 397.5, 399.2, 401.0, and 404.0 eV, corresponding to pyridinic N (N-6), pyrrolic N (N-5), graphitic N (N-Q), and oxidized N (N-O), respectively. N-5 and N-6 are known to be highly active towards K^+, leading to increased reversible capacity.[46,85] According to Table S3, the N content in SNCC and NCC is 1.36 and 1.39 wt%, respectively. However, according to Table S4, the content of N-5/N-6 is relatively higher in SNCC than in NCC, indicating that the S modifies the types of N moieties present. It has been reported that the adsorption energy of K ions at N/S codoping sites in defective graphene is higher than that at N-doping sites or at undoped sites.[86] It has also been reported that there is a synergistic electrical conductivity effect due to N/S codoping in carbons.[29] These two effects will combine with the more stable solid electrolyte interphase (SEI) and with improved solid-state diffusivity (demonstrated with simulation later in this paper) to allow for superior fast charge and cycling performance in SNCC versus the baseline NCC. According to Figures 3I and S5C, the high-resolution XPS O 1s spectrum of SNCC and NCC consists of three peaks, located at 532.3, 533.0, and 535.5 eV, representing C═O, C–OH/C–O–C, and COOH functional groups, respectively. These results are shown in Table S5. The SNCC has an extra peak located at 531.9 eV, corresponding to the O–S functional groups, respectively. The oxygen content in SNCC (10.44 wt%) is higher than that in NCC (8.19 wt%).

The electrochemical performances of SNCC and NCC were first investigated in half-cells versus potassium metal foils. Figure S6A shows the CV curves for the initial five cycles for SNCC, taken at 0.1 mV s^{-1}. The first scan shows an irreversible cathodic peak initiating near 1 V versus K/K^+, correlating to the formation of an SEI as well as some irreversible K ion trapping in the carbon.[16,61,85] During subsequent cycling, the broad cathodic peak with its maximum near 0.01 V has been associated with K ion intercalation, with the corresponding anodic peak having its maximum at 0.38 V.[61,87] In addition, SNCC shows another pair of peaks (0.75/0.6 V), which has been attributed to reversible K ion adsorption at the functional groups and associated defects in the carbon.[24,61] As shown in Figure S6B, the CV curves of NCC show similar features. However, the integrated area of CV curves for NCC is smaller than that of SNCC, indicating its lower reversible capacity.

Galvanostatic potassiation/depotassiation curves at 0.1 A g^{-1} are used to further evaluate the potassium storage behavior. These results are shown in Figure 4A,B. The initial potassiation/depotassiation capacities of SNCC and NCC are 579/400 and 468/293 mA h g^{-1}, respectively, with an associated ICE of 69.0% and 56.2%. The SNCC shows an irreversible plateau around 1 V in the first discharge process, which may be related to the formation of S-stabilized SEI and some irreversible trapping of K ions in carbon materials. According to Figure 4C and Table S6, both the reversible capacity and the ICE or SNCC are among the most favorable reported for K ion storing carbons.[6,24,29,45,88–97] This performance can be directly correlated to SNCC's unique structure: The relatively high (for K-ion storage) ICE is related to its low-surface area, which does not create excessive SEI, and its S doping, which is known to stabilize the K-based SEI of amorphous carbons.[24,98,99] The large reversible capacity is a cumulative effect due to multiple charge storage mechanisms, including reversible intercalation attributed to the dilated defective graphene,[25,46] as well as reversible adsorption at heteroatom moieties and the associated defects within the bulk carbon structure. It should be noted that for fast charging, the nanometer-scale solid-state diffusion distances in the bulk structure of SNCC are also key. These are enabled by sacrificial MgO templating. Short solid-state diffusion distances allow for maximum access of charge storage sites at the 0.1 A g^{-1} charging rate and become even more important at higher currents. In carbons where the solid-state diffusion distances are larger, such as in NCC, the intercalation and adsorption charge storage sites that are present will be less accessible.

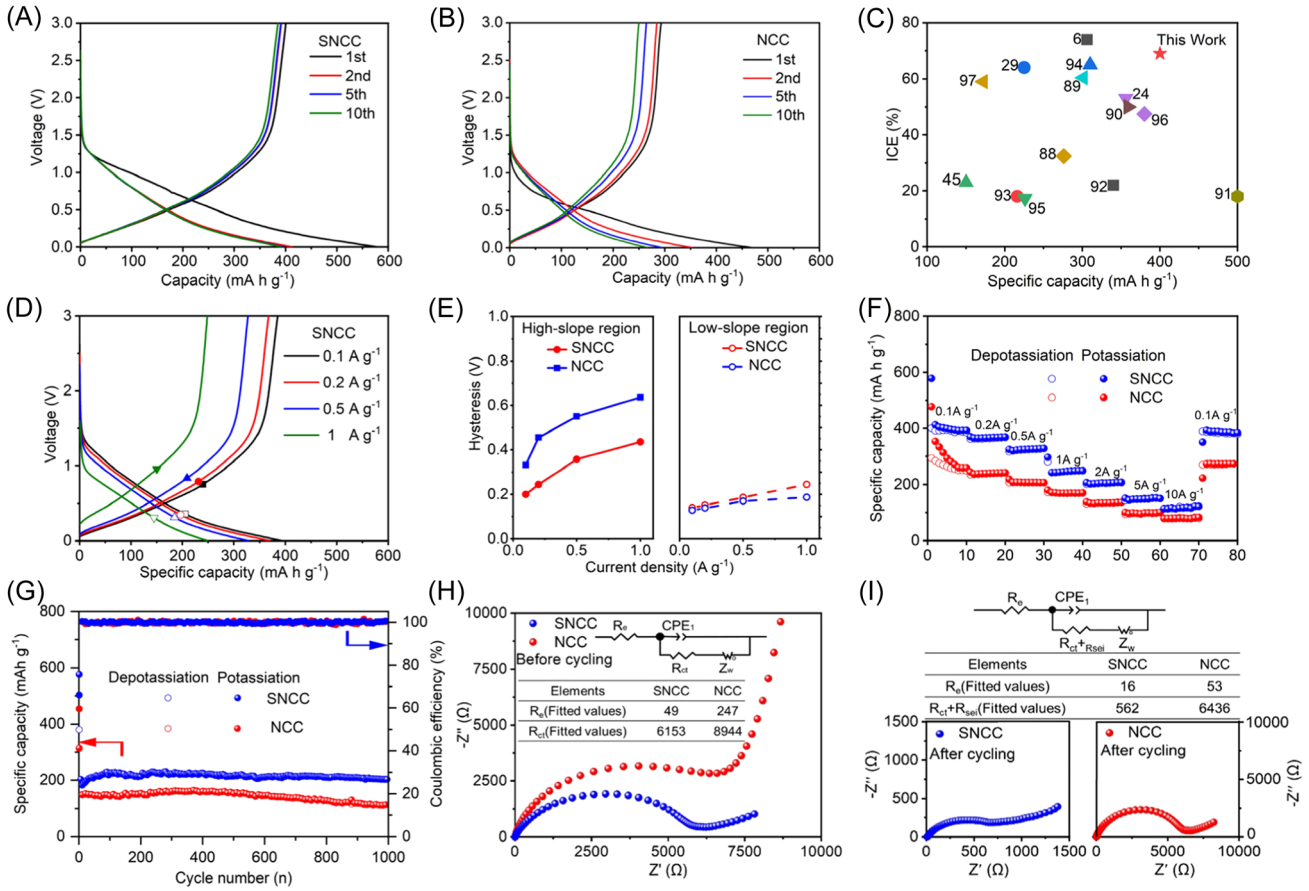

FIGURE 4 Galvanostatic potassiation/depotassiation curves of (A) SNCC and (B) baseline NCC, tested at 0.1 A g^{-1}. (C) Comparison of the specific capacity versus initial Coulombic efficiency for SNCC and state-of-the-art carbon-based potassium anode materials from the literature. (D) Galvanostatic curves for SNCC at different current densities, with sloping plateaus being subdividable into a high-voltage section and a low-voltage section. (E) Voltage hysteresis for the two sections, defined as the voltage difference between the respective potassiation/depotassiation curves at midpoint capacity. (F) Rate performance of SNCC and NCC. (G) Cycling performance of SNCC tested at 2 A g^{-1}. EIS of SNCC and NCC (H) before cycling and (I) after 1000 cycles. EIS, electrochemical impedance spectroscopy; NCC, N-doped cyanoethyl cellulose-derived carbon; SNCC, S, N codoped cyanoethyl cellulose-derived carbon.

To understand the SEI structure in SNCC, post-mortem XPS analysis was performed on specimens after Cycles 1 and 5. Analysis was performed on the carbons in the fully depotassiated state, meaning that any K-related peaks are due to irreversible reactions, primarily as part of the SEI formation. Figure S7 shows K 2p, S 2p, F 1s, and N 1s spectra. The K 2p after Cycle 1 shows two peaks at 293.4 and 296.2 eV, indicating the formation of K–C bonds.[100] Such K–C bonds can be attributed to the K_2CO_3 formed during the decomposition and reduction of carbon solvents, such as DME. The existence of K–S bonds indicates the formation of S-rich phases in the SEI. The peak at S 2p together with KSO_x (166.9 eV) and thiosulfate/–SO_2– (168.8 and 170.1 eV) is the main components of the SEI layer.[100] In addition, K–F (683.0 and 684.2 eV), C–F, O–F, and S–F (687.4 eV) are present in the F 1s.[101] In N 1s, N-5, N-6, and N-Q can be converted into N-5/K, N-6/K, and N-Q/K, respectively, indicating that the structure of the functional group had undergone irreversible changes.[24] In summary, XPS analysis demonstrates that the SEI film formed in SNCC is mainly composed of inorganic salts based on K–S, K–F, and K–C. The relative intensity, position, or shape of the peaks did not change significantly after Cycle 5, indicating that the SEI is stable. The CE of SNCC is substantially higher than that of NCC, and the XPS analysis helps to explain the electrochemical results. A stable SEI layer with SNCC will allow for rapid diffusion of K ions through it, enabling fast charge behavior.

The galvanostatic data may be analyzed further to gain insight regarding the charge storage behavior in SNCC versus NCC, following the analysis performed by Ji et al.[16] and Pint et al.,[23] as well as for Na ion storage in carbons with comparable structures.[102–105] According to Figure 4D, the galvanostatic curves may be roughly divided into two regions based on their slope. These

regions are related to the dominant charge storage mechanisms, with the lower-slope ion intercalation region denoted "L-slope" and the higher-voltage ion adsorption region denoted "H-slope." Figure S8 shows this analysis, with the two slopes being marked by dashed lines. It should be noted that the transition from L-slope to H-slope is somewhat gradual, which agrees with the two charge storage mechanisms operating in parallel and overlapping at intermediate potentials. With higher current density, the transition voltage between the two regions increases, indicating that ion adsorption becomes more dominant at faster charging. The potentials at the centers of the H- and L-slopes on the potassiation and depotassiation curves are marked as V_{DH}, V_{DL}, V_{CH}, and V_{CL}, and the hysteresis in H- and L-slope regions is calculated by determining the voltage difference between the corresponding potentials ($V_{CH} - V_{DH}$ and $V_{CL} - V_{DL}$).[106,107] The capacity contributions from L- and H-slope regions at various discharge rates are summarized in the bar chart in Figure S9.

The voltage hysteresis in both L- and H-slope regions as a function of potassiation/depotassiation current is shown in Figure 4E. At 0.1 A g^{-1}, NCC shows a voltage hysteresis of 0.33 V in the H-slope region and 0.14 V in the L-slope region, increasing to 0.55 and 0.18 V at 0.5 A g^{-1}, respectively. In SNCC, at 0.1 A g^{-1}, these values are 0.2 and 0.12 V, respectively, increasing to 0.35 and 0.17 V at 0.5 A g^{-1}. The difference in the overpotential behavior may be directly attributed to the shortened solid-state diffusion distances in SNCC, which in turn reduce the diffusional resistance of the electrode. As a secondary factor, a more stable SEI layer due to sulfur would also have an effect, reducing the SEI resistance during potassiation/depotassiation. This will be confirmed by the EIS analysis shown in the following discussion.

The comparisons of the rate capabilities of SNCC and NCC from 0.1 to 10 A g^{-1} are shown in Figure 4F. At current densities of 0.1, 0.2, 0.5, 1, 2, and 5 A g^{-1}, the SNCC electrode shows reversible capacities of 392, 369, 328, 249, 208, and 150 mA h g^{-1} (at Cycle 10), respectively. Even at 10 A g^{-1}, a reversible capacity of 121 mA h g^{-1} is achieved. When the current returns to 0.1 A g^{-1}, the capacity is recovered to 383 mA h g^{-1}. NCC shows significantly lower capacities at all currents, for example being 259 mA h g^{-1} at 0.1 A g^{-1} and 83 mA h g^{-1} at 10 A g^{-1}. The electrode's volumetric capacity is obtained by multiplying gravimetric capacity by the packing density, being 1.01 g cm^{-3} for SNCC and 1.07 g cm^{-3} for NCC. At current densities of 0.1, 0.2, 0.5, 1, 2, and 5 A g^{-1}, the volumetric capacities of SNCC are 396, 373, 331, 251, 210, 151, and 122 mA h cm^{-3}, respectively. As shown in Figure S10, the volumetric performance of SNCC is favorable relative to state-of-the-art carbon materials, although the number of reports focusing on capacity per volume is relatively limited.[25,62,108,109]

Extended cycling performance tests were carried out on SNCC and NCC, and the results are shown in Figure 4G. The initial 5 cycles were performed at 0.1 A g^{-1}, followed by 1000 cycles at 2 A g^{-1}. It may be observed that SNCC shows superior cycling stability to NCC. In summary, the enhanced rate capability and cycling stability of SNCC may be attributed to a combination of (i) thinner carbon walls and more dilated layer distance for improved solid-state diffusion, (ii) additional porosity for buffering of intercalation-induced volume changes, and (iii) more stable SEI layer due to S-doping, according to previous reports. The Cycle 6 reversible capacities of SNCC and NCC are 203.4 and 165.8 mA h g^{-1}, respectively. The Cycle 1000 reversible capacities of SNCC and NCC are 202.9 and 113.1 mA h g^{-1}, respectively, corresponding to 99.8% and 68.2% of the Cycle 6 reversible capacity values. It is well known that because of its large ionic size and the relatively less stable SEI layer, cycling of a range of carbons versus K/K^+ is more limited than versus Na/Na^+.[61,87,110] Relative to these results and considering the high density of SNCC, a 99.8% capacity retention after 1000 cycles may be considered good. It should be noted that not only is SNCC more stable than NCC in terms of relative capacity fade but it also operates at an overall higher capacity, and the difference increasing with cycle number. Figures 4H,I show the EIS Nyquist plots and the associated model fits of SNCC and NCC before cycling and after 1000 cycles. For NCC, the charge-transfer resistance (R_{ct}), combined with the resistance from the SEI layer (R_{sei}), is decreased from 8944 Ω before cycling to 6436 Ω after 1000 cycles. For SNCC, this combined resistance is significantly decreased from 6153 to 562 Ω. The reduced $R_{ct} + R_{sei}$ for SNCC is attributed to the electrode's S content, which promotes the progressive formation of a stable and inorganic phase-rich SEI during cycling. This effect was analyzed by XPS analysis shown earlier. The SEI in the baseline NCC also undergoes an activation process during cycling, lowering its overall resistance, but not to the same extent.

The diffusion coefficient of the K ions (D_K) can be estimated from the low-frequency region of the Nyquist plots according to the equation $D_K = 0.5R^2T^2/A^2n^4F^4C^2\sigma^2$.[111] In the equation, R is the gas constant, T represents the absolute temperature, A is the active surface area of the electrode/electrolyte interface, n is the number of transferred electrons, F is the Faraday constant, C is the bulk concentration, and σ is the Warburg coefficient, which is determined as the slope of Z versus $\omega^{-1/2}$ in the low-frequency region ($\sigma = d\acute{Z}/d\omega^{-1/2}$). The linear relationship between $\acute{Z}$ and $\omega^{-1/2}$ is shown in Figure S11, and the slope

σ is calculated. Therefore, the diffusion coefficients of K ions in SNCC and NCC before cycling were 7.08×10^{-15} and 2.36×10^{-15} $cm^2 s^{-1}$, respectively. As will be shown by the simulations, this difference is due to the dilated structure of SNCC, which facilitates rapid potassium diffusion. The diffusion coefficients of K in SNCC and NCC after cycling were 1.94×10^{-14} and 8.46×10^{-15} $cm^2 s^{-1}$, respectively. The increase in the diffusivity values may be attributed to additional lattice dilation due to the repeated insertion–extraction of potassium.

GITT measurements were performed on SNCC and NCC, as shown in Figure S12. The potential change in a complete pulse-relaxation procedure is shown in Figure S13. The calculated D_K values at differing potassiation depths are shown in Figure 5A. For both carbons, the D_K decreases with potassiation depth, which may be attributed to increased site occupancy and decreased driving force for additional ion insertion.[112,113] The D_K values for SNCC range from 1.3×10^{-11} to 3.7×10^{-13} $cm^2 s^{-1}$, an order of magnitude higher than the 1.1×10^{-12}–8×10^{-14} $cm^2 s^{-1}$ values for NCC. During depotassiation, the trend is reversed, with the maximum diffusivity at the onset voltage of ion extraction (Figure 5B). The ion sites that have the least driving force for insertion offer the most facile extraction kinetics. The D_K values for SNCC range from 4.1×10^{-11} to 1.8×10^{-12} $cm^2 s^{-1}$, an order of magnitude higher than the 3.2×10^{-12}–5.5×10^{-13} $cm^2 s^{-1}$ values for NCC. These results are consistent with the EIS analysis, with SNCC showing a higher D_K value than NCC over the entire potassiation/depotassiation process.

To further probe potassium storage mechanisms in SNCC, ex situ XRD was performed at a series of cutoff voltages. These results are shown in Figure 5C. During potassiation, additional peaks appeared on both sides of the (002) peak, revealing the formation of different potassium intercalation compounds (KICs) in the form of KC_x. The KC_{36} (22.0°/29.4°) phases first appeared below 0.5 V, indicating that charge storage above this cutoff is due to reversible ion adsorption in chemical and structural defects. Upon further potassiation to 0.15 V, KC_{24} (20.2°/30.6°) and KC_8 (15.9°/33.1°) KICs are produced. This process is similar to the low-voltage K intercalation reaction into graphite. At a terminally potassiated state at 0.001 V, only the KC_8 phase is detected. During the depotassiation process, at a voltage

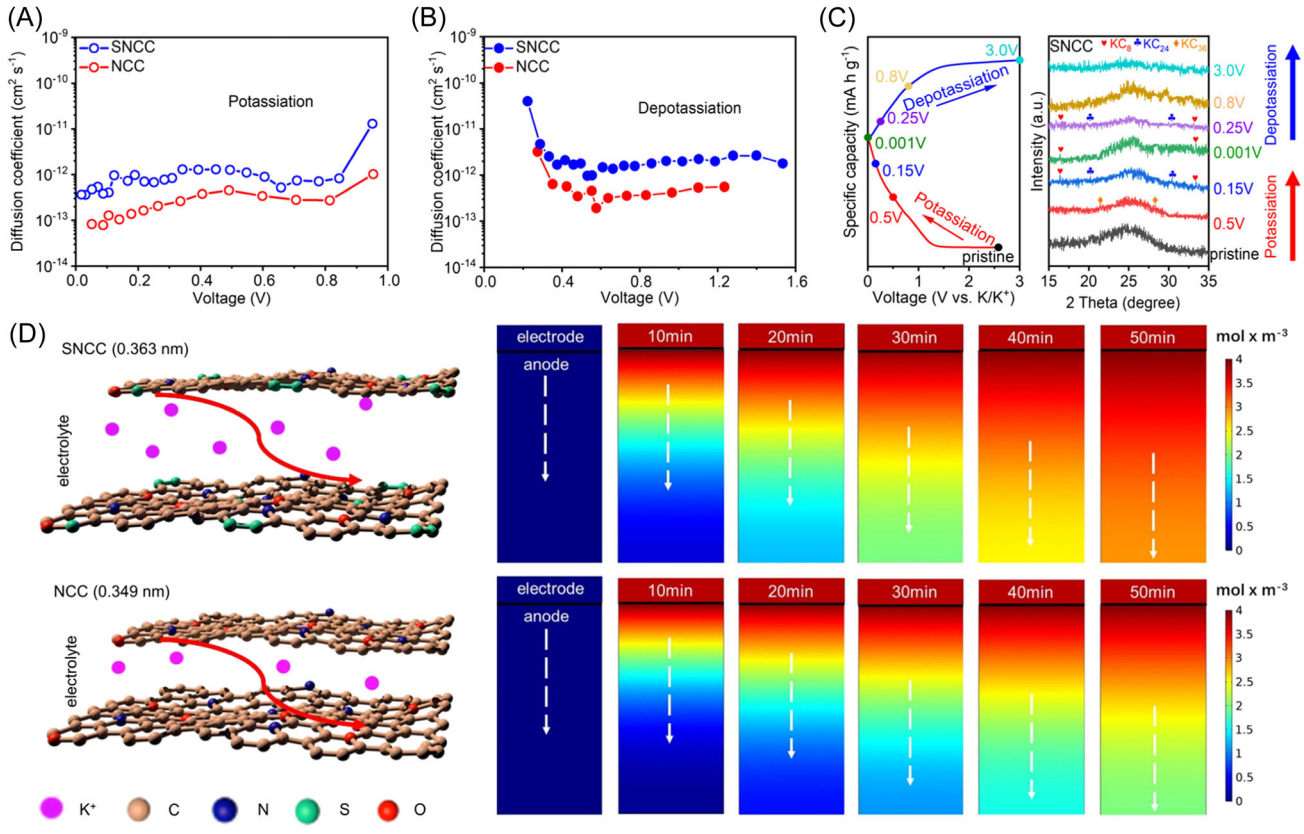

FIGURE 5 (A) Potassiation-derived diffusion coefficients of K^+ in SNCC and NCC. (B) Depotassiation-derived diffusion coefficients of K^+ in SNCC and NCC. (C) Ex situ XRD analysis of SNCC. (D) COMSOL Multiphysics simulations of K^+ transport kinetics in SNCC (top) and NCC (bottom) anodes at different potassiation times. NCC, N-doped cyanoethyl cellulose-derived carbon; SNCC, S, N codoped cyanoethyl cellulose-derived carbon; XRD, X-ray diffraction.

of 0.25 V, the KC_{24} phase appears again. As the voltage increases to 0.8 V, the peaks associated with the KC_x compounds disappear. These results confirm that ion intercalation occurs primarily in the low-voltage region. It should be noted that XRD cannot detect ion adsorption at defects, which does not produce crystallographic potassium–carbon compounds. Therefore, it is not possible to specify the lower voltage at which reversible ion adsorption ceases to be an important contributor to the total reversible capacity.

To analyze the role of the dilated graphene layer distance (0.363 nm for SNCC vs. 0.349 nm for NCC) on the electrochemical performance, COMSOL Multiphysics simulation modeling was performed. The details of the simulation are provided in Section 2. Figure 5D shows the evolution of K^+ concentration in the structures during the potassiation process, reflecting the corresponding K^+ diffusion kinetics. With an increase of the layer distance, the potassium concentration in the bottom region of the SNCC reached 50% of that in the top region within 30 min. By contrast, in the NCC anode, this process took 50 min. After 50 min, the ratio of the K^+ concentration in the bottom region to the concentration in the top region of SNCC was greater than that of NCC, being at 75% versus 50%. In summary, the simulation shows that the expanded layer distance (everything else being kept equal) will significantly enhance solid-state diffusion of K^+.

To demonstrate a full-cell application of the SNCC, PICs were assembled by using SNCC as the anode and NS-PC as the cathode. These results are shown in Figure 6A. The capacity of the cathode electrode primarily comes from the reversible adsorption of FSI^-, although some high-voltage surface adsorption and redox reactions may also make contributions.[114] The electrochemical performance of the NS-PC cathode is shown in Figure S14. As shown in Figure S15, the PICs fabricated with an anode-to-cathode mass ratio of 1:3 show the best energy and power characteristics. Figures S16 and 6B show the CV curves and the potassiation/depotassiation profiles of such PICs, respectively. To provide a broad comparison, Figure 6C illustrates the comparison of energy and powder characteristics of the SNCC//NS-PC PICs and previously reported devices, demonstrating the highly favorable energy and power characteristics of the SNCC//NS-PC PICs.[61,115–124] Figure 6D shows that the SNCC//NS-PC PICs can sustain over 6000 cycles at 30 A g^{-1} with a capacity retention of 84.5%. Figure 6E shows EIS analysis that may be used to further understand the cycling performance of this PICs. After 6000 cycles, the equivalent series resistance (R_s) is stable, increasing minimally from 8.01 Ω before cycling to

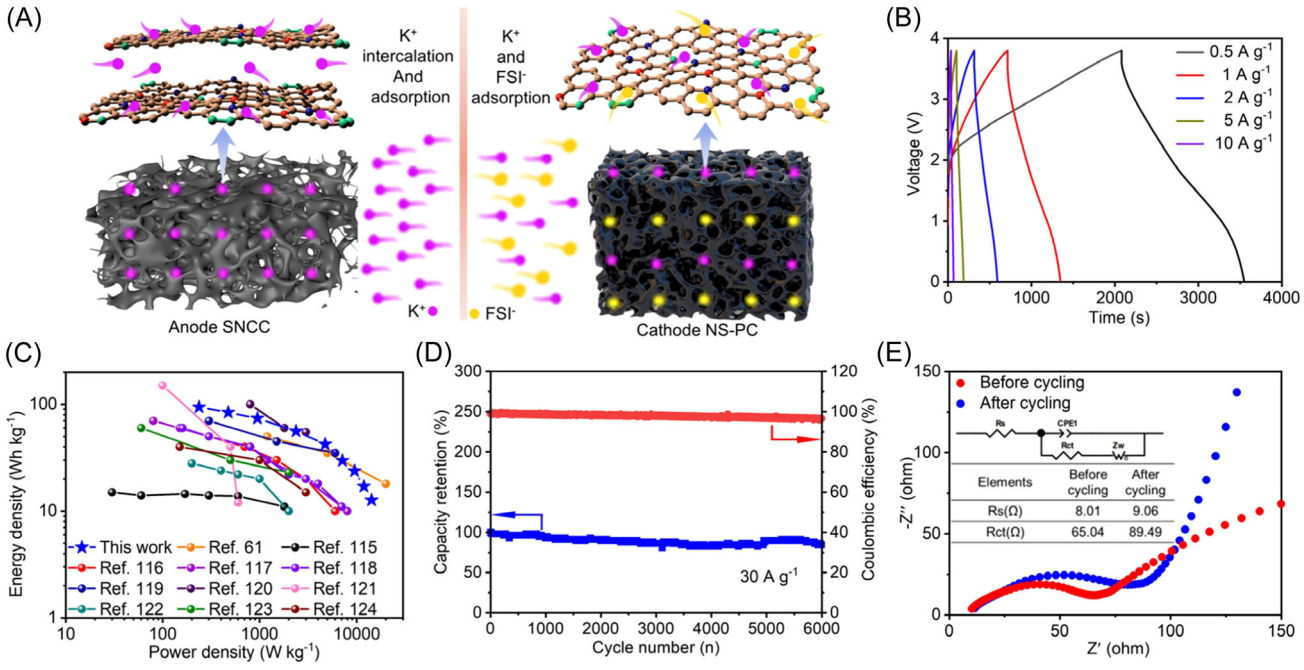

FIGURE 6 Electrochemical performance of a potassium ion capacitor based on an SNCC anode and an NS-PC cathode. (A) Schematic illustration of the PICs device. (B) Galvanostatic potassiation/depotassiation profiles of the SNCC//NS-PC PICs, tested at currents ranging from 0.5 to 10 A g^{-1}. (C) Ragone plots of SNCC//NS-PC PICs comparing them with state-of-the-art PICs from the literature. (D) Long-term cycling performance and (E) Nyquist plots of SNCC//NS-PC PICs, tested at 30 A g^{-1}. NS-PC, N, S codoped porous carbon; PIC, potassium ion capacitor; SNCC, S, N codoped cyanoethyl cellulose-derived carbon.

9.06 Ω after cycling. Likewise, the R_{ct} values are relatively stable, increasing from 65.04 to 89.49 Ω after 6000 cycles. These results reveal that full cells using SNCC show stable microstructures that do not degrade during cycling or develop unstable SEI characteristics.

4 | CONCLUSIONS

In summary, we report a scalable synthesis approach to fabricate dense, low-surface-area carbons with state-of-the-art performance as PICs or PIB anodes. Fabrication of SNCC mimics a commercial process for the manufacture of viscose (a low-cost silk substitute), followed by direct carbonization without any activation agents. The internal structure of SNCC is based on highly dilated and defective graphene sheets arranged into nanometer-scale walls, leading to rapid solid-state diffusion according to GITT analysis and COMSOL simulations. SNCC shows reversible capacities of 392, 369, 328, 249, 208, 150, and 121 mA h g^{-1} at current densities of 0.1, 0.2, 0.5, 1, 2, 5, and 10 A g^{-1}, respectively. At these currents, SNCC delivers volumetric capacities of 396, 373, 331, 251, 210, 151, and 122 mA h cm^{-3}, respectively. A broad comparison with the state-of-the-art literature on carbon anodes for potassium indicates that this combination of gravimetric and volumetric performance is among the most competitive. Moreover, due to its low-surface area (21.2 m^2 g^{-1}) and a S-stabilized SEI, SNCC shows promising ICE (69.0%) and extended cycling stability (99.8% capacity retention after 1000 cycles). As proof of principle, an SNCC-based PIC shows favorable Ragone chart characteristics, for example, 94.3 Wh kg^{-1} at 237.5 W kg^{-1}, and sustains over 6000 cycles at 30 A g^{-1} with a capacity retention of 84.5%.

ACKNOWLEDGMENTS

Guangzeng Cheng, Wenzhe Zhang, and Wei Wang contributed equally to this study. Guangzeng Cheng, Wenzhe Zhang, Wei Wang, Huanlei Wang, Jing Shi, Jingwei Chen, Shuai Liu, and Minghua Huang (who contributed to the conception of research, synthesis and experimental/theoretical analysis, and copreparation of the manuscript) were supported by the National Natural Science Foundation of China (Grant Nos. 22179123 and 21471139), the Shandong Provincial Natural Science Foundation, China (Grant No. ZR2020ME038), and the Fundamental Research Funds for the Central Universities (Grant No. 201941010). David Mitlin and Yixian Wang (who contributed toward research coconception and guidance, and manuscript preparation) were supported by the National Science Foundation, Division of Materials Research, Award Number 1938833.

CONFLICT OF INTEREST

The authors declare that there are no conflict of interests.

ORCID

Huanlei Wang http://orcid.org/0000-0001-8218-1762
Yixian Wang http://orcid.org/0000-0001-6107-8352
David Mitlin http://orcid.org/0000-0002-7556-3575

REFERENCES

1. Guan C, Zhao W, Hu Y, et al. High-performance flexible solid-state Ni/Fe battery consisting of metal oxides coated carbon cloth/carbon nanofiber electrodes. *Adv Energy Mater*. 2016;6(20):1601034.
2. Simon P, Gogotsi Y. Materials for electrochemical capacitors. *Nat Mater*. 2008;7(11):845-854.
3. Liu Y, Yang C, Pan Q, et al. Nitrogen-doped bamboo-like carbon nanotubes as anode material for high performance potassium ion batteries. *J Mater Chem A*. 2018;6(31):15162-15169.
4. Yang D, Liu C, Rui X, Yan Q. Embracing high performance potassium-ion batteries with phosphorus-based electrodes: a review. *Nanoscale*. 2019;11(33):15402-15417.
5. Liu Y, He D, Tan Q, et al. A synergetic strategy for an advanced electrode with Fe_3O_4 embedded in a 3D N-doped porous graphene framework and a strong adhesive binder for lithium/potassium ion batteries with an ultralong cycle lifespan. *J Mater Chem A*. 2019;7(33):19430-19441.
6. Yang W, Zhou J, Wang S, et al. A three-dimensional carbon framework constructed by N/S co-doped graphene nanosheets with expanded interlayer spacing facilitates potassium ion storage. *ACS Energy Lett*. 2020;5(5):1653-1661.
7. Bruce PG, Scrosati B, Tarascon JM. Nanomaterials for rechargeable lithium batteries. *Angew Chem Int Ed*. 2008;47(16):2930-2946.
8. Mo R, Li F, Tan X, et al. High-quality mesoporous graphene particles as high-energy and fast-charging anodes for lithium-ion batteries. *Nat Commun*. 2019;10:1474.
9. Shang J, Dong H, Geng H, et al. Electronic modulation of nickel selenide by copper doping and in situ carbon coating towards high-rate and high-energy density lithium ion half/full batteries. *Nanoscale*. 2020;12(46):23645-23652.
10. Sun X, Jin Y, Wang H, et al. Chemically activated hollow carbon nanospheres as a high-performance anode material for potassium ion batteries. *J Mater Chem A*. 2018;6(47):24317-24323.
11. Yang M, Kong Q, Feng W, Yao W, Wang Q. Hierarchical porous nitrogen, oxygen, and phosphorus ternary doped hollow biomass carbon spheres for high-speed and long-life potassium storage. *Carbon Energy*. 2022;4(1):45-59.
12. Zhu Z, Zhong W, Zhang Y, et al. Elucidating electrochemical intercalation mechanisms of biomass-derived hard carbon in sodium-/potassium-ion batteries. *Carbon Energy*. 2021;3(4):541-553.
13. Ruan J, Wu X, Wang Y, et al. Nitrogen-doped hollow carbon nanospheres towards the application of potassium ion storage. *J Mater Chem A*. 2019;7(33):19305-19315.
14. Wen Y, He K, Zhu Y, et al. Expanded graphite as superior anode for sodium-ion batteries. *Nat Commun*. 2014;5:4033.

15. Bai J, Xi B, Mao H, et al. One-step construction of N,P-codoped porous carbon sheets/CoP hybrids with enhanced lithium and potassium storage. *Adv Mater*. 2018;30(35):1802310.
16. Jian Z, Luo W, Ji X. Carbon electrodes for K-ion batteries. *J Am Chem Soc*. 2015;137(36):11566-11569.
17. Zhu YH, Yin YB, Yang X, et al. Transformation of rusty stainless-steel meshes into stable, low-cost, and binder-free cathodes for high-performance potassium-ion batteries. *Angew Chem Int Ed*. 2017;56(27):7881-7885.
18. Song F, Hu J, Li G, et al. Sulfur-assisted large-scale synthesis of graphene microspheres for superior potassium-ion batteries. *Energy Environ Sci*. 2021;14(2):965-974.
19. Alvin S, Cahyadi HS, Hwang J, Chang W, Kwak SK, Kim J. Revealing the intercalation mechanisms of lithium, sodium, and potassium in hard carbon. *Adv Energy Mater*. 2020;10(20):2000283.
20. Zhao X, Song Y, Liu Z. Kinetics enhanced hierarchical $Ni_2P_{1-x}S_x$/Ni@carbon/graphene yolk-shell microspheres boosting advanced sodium/potassium storage. *J Mater Chem A*. 2020;8(45):23994-24004.
21. Fan L, Ma R, Zhang Q, Jia X, Lu B. Surface-substituted prussian blue analogue cathode for sustainable potassium-ion batteries. *Nat Sustain*. 2022;5(3):225-234.
22. Ge J, Fan L, Rao AM, Zhou J, Lu B. Graphite anode for a potassium-ion battery with unprecedented performance. *Angew Chem Int Ed*. 2019;58(31):10500-10505.
23. Share K, Cohn AP, Carter R, Rogers B, Pint CL. Role of nitrogen-doped graphene for improved high-capacity potassium ion battery anodes. *ACS Nano*. 2016;10(10):9738-9744.
24. Tao L, Yang Y, Wang H, et al. Sulfur-nitrogen rich carbon as stable high capacity potassium ion battery anode: performance and storage mechanisms. *Energy Storage Mater*. 2020;27:212-225.
25. Sun Y, Wang H, Wei W, et al. Sulfur-rich graphene nanoboxes with ultra-high potassiation capacity at fast charge: storage mechanisms and device performance. *ACS Nano*. 2021;15(1):1652-1665.
26. Peng D, Chen Y, Ma H, et al. Enhancing the cycling stability by tuning the chemical bonding between phosphorus and carbon nanotubes for potassium-ion battery anodes. *ACS Appl Mater Interfaces*. 2020;12(33):37275-37284.
27. Peng S, Wang L, Zhu Z, Han K. Electrochemical performance of reduced graphene oxide/carbon nanotube hybrid papers as binder-free anodes for potassium-ion batteries. *J Phys Chem Solids*. 2020;138:109296.
28. Tai Z, Zhang Q, Liu Y, Liu H, Dou S. Activated carbon from the graphite with increased rate capability for the potassium ion battery. *Carbon*. 2017;123:54-61.
29. Lv C, Xu W, Liu H, et al. 3D sulfur and nitrogen codoped carbon nanofiber aerogels with optimized electronic structure and enlarged interlayer spacing boost potassium-ion storage. *Small*. 2019;15(23):1900816.
30. Qin G, Liu Y, Liu F, et al. Magnetic field assisted construction of hollow red P nanospheres confined in hierarchical N-doped carbon nanosheets/nanotubes 3D framework for efficient potassium storage. *Adv Energy Mater*. 2021;11(4):2003429.
31. Tao XS, Sun YG, Liu Y, et al. Facile synthesis of hollow carbon nanospheres and their potential as stable anode materials in potassium-ion batteries. *ACS Appl Mater Interfaces*. 2020;12(11):13182-13188.
32. Wang T, Liu W, Gao X, et al. Fe nanopowder-assisted fabrication of FeO_x/porous carbon for boosting potassium-ion storage performance. *Nanoscale*. 2021;13(4):2481-2491.
33. Liu Y, Huang B, Zheng L, et al. UIO-66-NH_2-derived mesoporous carbon used as a high-performance anode for the potassium-ion battery. *RSC Adv*. 2021;11(2):1039-1049.
34. Wang M, Zhu Y, Zhang Y, Yang T, Duan J, Wang C. Cost-effective hard-soft carbon composite anodes with promising potassium ions storage performance. *Electrochim Acta*. 2021;368:137649.
35. Wang T, Shen D, Liu H, Chen H, Liu Q, Lu B. A Sb_2S_3 Nanoflower/MXene composite as an anode for potassium-ion batteries. *ACS Appl Mater Interfaces*. 2020;12(52):57907-57915.
36. Xia J, Liu L, Jamil S, et al. Free-standing SnS/C nanofiber anodes for ultralong cycle-life lithium-ion batteries and sodium-ion batteries. *Energy Storage Mater*. 2019;17:1-11.
37. Shen JK, Every J, Morrison SD, Massenburg BB, Egbert MA, Susarla SM. An in-depth study of heteroatom boosted anode for potassium-ion batteries. *Nano Energy*. 2020;78:105294.
38. Qian Y, Li Y, Yi Z, et al. Revealing the double-edged behaviors of heteroatom sulfur in carbonaceous materials for balancing K-storage capacity and stability. *Adv Funct Mater*. 2021;31(8):2006875.
39. Jiang P, Fan YV, Klemeš JJ. High-performance potassium ion capacitors enabled by hierarchical porous, large interlayer spacing, active site rich-nitrogen, and sulfur co-doped carbon. *Carbon*. 2020;164:1-11.
40. Tao L, Liu L, Chang R, He H, Zhao P, Liu J. Structural and interface design of hierarchical porous carbon derived from soybeans as anode materials for potassium-ion batteries. *J Power Sources*. 2020;463:228172.
41. Wang D, Tian KH, Wang J, et al. Sulfur-doped 3D hierarchical porous carbon network toward excellent potassium-ion storage performance. *Rare Met*. 2021;40(9):2464-2473.
42. Chen J, Yang B, Hou H, et al. Disordered, large interlayer spacing, and oxygen-rich carbon nanosheets for potassium ion hybrid capacitor. *Adv Energy Mater*. 2019;9(19):1803894.
43. Chen J, Yang B, Li H, Ma P, Lang J, Yang X. Candle soot: onion-like carbon, an advanced anode material for a potassium-ion hybrid capacitor. *J Mater Chem A*. 2019;7(15):9247-9252.
44. Mahmood A, Li S, Ali Z, et al. Ultrafast sodium/potassium-ion intercalation into hierarchically porous thin carbon shells. *Adv Mater*. 2019;31(2):1805430.
45. Chen M, Wang W, Liang X, et al. Sulfur/oxygen codoped porous hard carbon microspheres for high-performance potassium-ion batteries. *Adv Energy Mater*. 2018;8(19):1800171.
46. Yang J, Ju Z, Jiang Y, et al. Enhanced capacity and rate capability of nitrogen/oxygen dual-doped hard carbon in capacitive potassium-ion storage. *Adv Mater*. 2018;30(4):1700104.

47. Lee B, Kim M, Kim S, et al. High capacity adsorption-dominated potassium and sodium ion storage in activated crumpled graphene. *Adv Energy Mater*. 2020;10(17):1903280.
48. Xu Y, Xue M, Li J, Zhang L, Cui Y. Synthesis of a cellulose xanthate supported palladium(0) complex and its catalytic behavior in the heck reaction. *React Kinet Mech Catal*. 2010;100(2):347-353.
49. Zhang Y, Luo C, Wang H, et al. Modified adsorbent hydroxypropyl cellulose xanthate for removal of Cu^{2+} and Ni^{2+} from aqueous solution. *Desalin Water Treat*. 2016; 57(56):27419-27431.
50. Chen L, Liu S, Wang Y, et al. Ortho-di-sodium salts of tetrahydroxyquinone as a novel electrode for lithium-ion and potassium-ion batteries. *Electrochim Acta*. 2019;294:46-52.
51. Zhao J, Yang J, Sun P, Xu Y. Sodium sulfonate groups substituted anthraquinone as an organic cathode for potassium batteries. *Electrochem Commun*. 2018;86:34-37.
52. Saito T, Kimura S, Nishiyama Y, Isogai A. Cellulose nanofibers prepared by TEMPO-mediated oxidation of native cellulose. *Biomacromolecules*. 2007;8(8):2485-2491.
53. Wang C, Wang H, Gu G. Ultrasound-assisted xanthation of cellulose from lignocellulosic biomass optimized by response surface methodology for Pb(II) sorption. *Carbohydr Polym*. 2018;182:21-28.
54. Pan Q, Liu W, Ma M, et al. Preparation of rice straw cellulose xanthate and study on its adsorption properties of cadmium (II) from aqueous solutions. *Asian J Chem*. 2014;26(2): 562-564.
55. Kuang Y, Chen C, Pastel G, et al. Conductive cellulose nanofiber enabled thick electrode for compact and flexible energy storage devices. *Adv Energy Mater*. 2018;8(33):1802398.
56. Li Y, Zhu H, Shen F, et al. Highly conductive microfiber of graphene oxide templated carbonization of nanofibrillated cellulose. *Adv Funct Mater*. 2014;24(46):7366-7372.
57. Xu D, Chen C, Xie J, et al. A hierarchical N/S-codoped carbon anode fabricated facilely from cellulose/polyaniline microspheres for high-performance sodium-ion batteries. *Adv Energy Mater*. 2016;6(6):1501929.
58. Dacrory S, Fahim AM. Synthesis, anti-proliferative activity, computational studies of tetrazole cellulose utilizing different homogenous catalyst. *Carbohydr Polym*. 2020;229:115537.
59. Dacrory S, Abou HAB, Nahrawy AMEl, Abou-Yousef H, Kamel S. Cyanoethyl cellulose/$BaTiO_3$/GO flexible films with electroconductive properties. *ECS J Solid State Sci Technol*. 2021;10(8):083004.
60. Ding J, Zhang H, Zhou H, et al. Sulfur-grafted hollow carbon spheres for potassium-ion battery anodes. *Adv Mater*. 2019;31(30):1900429.
61. Xu Z, Wu M, Chen Z, et al. Direct structure-performance comparison of all-carbon potassium and sodium ion capacitors. *Adv Sci*. 2019;6(12):1802272.
62. Han J, Zhang C, Kong D, et al. Flowable sulfur template induced fully interconnected pore structures in graphene artefacts towards high volumetric potassium storage. *Nano Energy*. 2020;72:104729.
63. Zhang Z, Jia B, Liu L, et al. Hollow multihole carbon bowls: a stress-release structure design for high-stability and high-volumetric-capacity potassium-ion batteries. *ACS Nano*. 2019;13(10):11363-11371.
64. Shaikh T, Chaudhari S, Varma A. Viscose rayon: a legendary development in the manmade textile. *Int J Eng Res Appl*. 2012;2(5):675-680.
65. Sayyed AJ, Deshmukh NA, Pinjari DV. A critical review of manufacturing processes used in regenerated cellulosic fibres: viscose, cellulose acetate, cuprammonium, LiCl/DMAc, ionic liquids, and NMMO based lyocell. *Cellulose*. 2019;26(5):2913-2940.
66. Roy Choudhury AK. *Textile Preparation and Dyeing*. Science Publishers; 2006.
67. Cassidy T, Goswami P. *Textile and Clothing Design Technology*. CRC Press; 2017.
68. Piao C, Wu J, Cui ML. Water-soluble salt template-assisted anchor of hollow FeS_2 nanoparticle inside 3D carbon skeleton to achieve fast potassium-ion storage. *Adv Energy Mater*. 2021;11(33):2101343.
69. Zhao CZ, Chen PY, Zhang R, et al. An ion redistributor for dendrite-free lithium metal anodes. *Sci Adv*. 2018;4(11):eaat3446.
70. Deng P, Sheng W, Xu A, et al. Ion-transport-rectifying layer enables Li-metal batteries with high energy density. *Matter*. 2020;3(5):1685-1700.
71. Beyki MH, Bayat M, Miri S, Shemirani F, Alijani H. Synthesis, characterization, and silver adsorption property of magnetic cellulose xanthate from acidic solution: prepared by one step and biogenic approach. *Ind Eng Chem Res*. 2014;53(39):14904-14912.
72. Liu Y, Xue J, Zheng T, Dahn JR. Mechanism of lithium insertion in hard carbons prepared by pyrolysis of epoxy resins. *Carbon*. 1996;34(2):193-200.
73. Su D, Maksimova NI, Mestl G, et al. Oxidative dehydrogenation of ethylbenzene to styrene over ultra-dispersed diamond and onion-like carbon. *Carbon*. 2007; 45(11):2145-2151.
74. Zhou H, Yu WJ, Liu L, et al. Chemical vapour deposition growth of large single crystals of monolayer and bilayer graphene. *Nat Commun*. 2013;4:2096.
75. Yang P, Zou X, Zhang Z, et al. Batch production of 6-inch uniform monolayer molybdenum disulfide catalyzed by sodium in glass. *Nat Commun*. 2018;9:979.
76. Li X, Wang H, Zhang W, et al. High potassium ion storage capacity with long cycling stability of sustainable oxygen-rich carbon nanosheets. *Nanoscale*. 2021;13(4):2389-2398.
77. Takami N, Satoh A, Oguchi M, Sasaki H, Ohsaki T. ^{7}Li NMR and ESR analysis of lithium storage in a high-capacity perylene-based disordered carbon. *J Power Sources*. 1997; 68(2):283-286.
78. Zhang B, Ghimbeu CM, Laberty C, Vix-Guterl C, Tarascon JM. Correlation between microstructure and Na storage behavior in hard carbon. *Adv Energy Mater*. 2016;6(1):1501588.
79. Chen C, Wu M, Wang Y, Zaghin K. Insights into pseudographite-structured hard carbon with stabilized performance for high energy K-ion storage. *J Power Sources*. 2019;444:227310.
80. Yushin G, Dash R, Jagiello J, Fischer JE, Gogotsi Y. Carbide-derived carbons: effect of pore size on hydrogen uptake and heat of adsorption. *Adv Funct Mater*. 2006;16(17):2288-2293.
81. Gogotsi Y, Portet C, Osswald S, et al. Importance of pore size in high-pressure hydrogen storage by porous carbons. *Int J Hydrogen Energy*. 2009;34(15):6314-6319.

82. Cui Y, Liu W, Wang X, et al. Bioinspired mineralization under freezing conditions: an approach to fabricate porous carbons with complicated architecture and superior K^+ storage performance. *ACS Nano*. 2019;13(10):11582-11592.
83. Xu C, Han Q, Zhao Y, Wang L, Li Y, Qu L. Sulfur-doped graphitic carbon nitride decorated with graphene quantum dots for an efficient metal-free electrocatalyst. *J Mater Chem A*. 2015;3(5):1841-1846.
84. Tian S, Guan D, Lu J, et al. Synthesis of the electrochemically stable sulfur-doped bamboo charcoal as the anode material of potassium-ion batteries. *J Power Sources*. 2020;448:227572.
85. Zhang W, Ming J, Zhao W, et al. Graphitic nanocarbon with engineered defects for high-performance potassium-ion battery anodes. *Adv Funct Mater*. 2019;29(35):1903641.
86. Chen Y, Xi B, Huang M, et al. Defect-selectivity and "order-in-disorder" engineering in carbon for durable and fast potassium storage. *Adv Mater*. 2022;34(7):2108621.
87. Jian Z, Xing Z, Bommier C, Li Z, Ji X. Hard carbon microspheres: potassium-ion anode versus sodium-ion anode. *Adv Energy Mater*. 2016;6(3):1501874.
88. Ge L, Chen Y, Yan C, et al. A large scalable and low-cost sulfur/nitrogen dual-doped hard carbon as the negative electrode material for high-performance potassium-ion batteries. *Adv Energy Mater*. 2019;9(34):1901379.
89. Ma X, Xiao N, Xiao J, et al. Nitrogen and phosphorus dual-doped porous carbons for high-rate potassium ion batteries. *Carbon*. 2021;179:33-41.
90. Liu Q, Han F, Zhou J, et al. Boosting the potassium-ion storage performance in soft carbon anodes by the synergistic effect of optimized molten salt medium and N/S dual-doping. *ACS Appl Mater Interfaces*. 2020;12(18):20838-20848.
91. Lu X, Fang M, Yang Y, et al. Enhanced kinetics harvested in heteroatom dual-doped graphitic hollow architectures toward high rate printable potassium-ion batteries. *Adv Energy Mater*. 2020;10(28):2001161.
92. Chen S, Feng Y, Wang J, Zhang E, Yu X, Lu B. Free-standing N-doped hollow carbon fibers as high-performance anode for potassium ion batteries. *Sci China Mater*. 2021;64(3):547-556.
93. Li J, Yu L, Li Y, et al. Phosphorus-doping-induced kinetics modulation for nitrogen-doped carbon mesoporous nanotubes as superior alkali metal anode beyond lithium for high-energy potassium-ion hybrid capacitors. *Nanoscale*. 2021;13(2):692-699.
94. Li D, Cheng X, Xu R, et al. Manipulation of 2D carbon nanoplates with a core-shell structure for high-performance potassium-ion batteries. *J Mater Chem A*. 2019;7(34):19929-19938.
95. Zeng S, Zhou X, Wang B, et al. Freestanding CNT-modified graphitic carbon foam as a flexible anode for potassium ion batteries. *J Mater Chem A*. 2019;7(26):15774-15781.
96. Wu Z, Wang L, Huang J, et al. Loofah-derived carbon as an anode material for potassium ion and lithium ion batteries. *Electrochim Acta*. 2019;306:446-453.
97. Wang H, Yang G, Chen Z, et al. Nitrogen configuration dependent holey active sites toward enhanced K^+ storage in graphite foam. *J Power Sources*. 2019;419:82-90.
98. Bi H, He X, Yang L, Li H, Jin B, Qiu J. Interconnected carbon nanocapsules with high N/S co-doping as stable and high-capacity potassium-ion battery anode. *J Energy Chem*. 2022;66:195-204.
99. Liu X, Tong Y, Wu Y, et al. Synergistically enhanced electrochemical performance using nitrogen, phosphorus and sulfur tri-doped hollow carbon for advanced potassium ion storage device. *Chem Eng J*. 2022;431:133986.
100. Li J, Qin W, Xie J, et al. Sulphur-doped reduced graphene oxide sponges as high-performance free-standing anodes for K-ion storage. *Nano Energy*. 2018;53:415-424.
101. Gao X, Dong X, Xing Z, Nie C, Zheng G, Ju Z. Electrolyte salt chemistry enables 3D nitrogen and phosphorus dual-doped graphene aerogels for high-performance potassium-ion batteries. *Adv Mater Technol*. 2021;6(8):2100207.
102. Ding J, Wang H, Li Z, et al. Carbon nanosheet frameworks derived from peat moss as high performance sodium ion battery anodes. *ACS Nano*. 2013;7(12):11004-11015.
103. Lotfabad EM, Ding J, Cui K, et al. High-density sodium and lithium ion battery anodes from banana peels. *ACS Nano*. 2014;8(7):7115-7129.
104. Ding J, Wang H, Li Z, et al. Peanut shell hybrid sodium ion capacitor with extreme energy-power rivals lithium ion capacitors. *Energy Environ Sci*. 2015;8(3):941-955.
105. Bommier C, Mitlin D, Ji X. Internal structure-Na storage mechanisms-electrochemical performance relations in carbons. *Prog Mater Sci*. 2018;97:170-203.
106. Bommier C, Surta TW, Dolgos M, Ji X. New mechanistic Insights on Na-ion storage in nongraphitizable carbon. *Nano Lett*. 2015;15(9):5888-5892.
107. Fu L, Tang K, Song K, Aken PAV, Yu Y, Maier J. Nitrogen doped porous carbon fibres as anode materials for sodium ion batteries with excellent rate performance. *Nanoscale*. 2014;6(3):1384-1389.
108. Vaalma C, Giffin GA, Buchholz D, Passerini S. Non-aqueous K-ion battery based on layered $K_{0.3}MnO_2$ and hard carbon/carbon black. *J Electrochem Soc*. 2016;163(7):A1295-A1299.
109. Tan H, Zhou R, Zhang B. Understanding potassium ion storage mechanism in pitch-derived soft carbon and the consequence on cyclic stability. *J Power Sources*. 2021;506:230179.
110. Liu X, Elia GA, Qin B, et al. High-power Na-ion and K-ion hybrid capacitors exploiting cointercalation in graphite negative electrodes. *ACS Energy Lett*. 2019;4(11):2675-2682.
111. Wang W, Zhou J, Wang Z, et al. Short-range order in mesoporous carbon boosts potassium-ion battery performance. *Adv Energy Mater*. 2018;8(5):1701648.
112. Qiu D, Kang C, Li M, et al. Biomass-derived mesopore-dominant hierarchical porous carbon enabling ultra-efficient lithium ion storage. *Carbon*. 2020;162:595-603.
113. Tang K, Yu X, Sun J, Li H, Huang X. Kinetic analysis on $LiFePO_4$ thin films by CV, GITT, and EIS. *Electrochim Acta*. 2011;56(13):4869-4875.
114. Dou Q, Wu N, Yuan H, et al. Emerging trends in anion storage materials for the capacitive and hybrid energy storage and beyond. *Chem Soc Rev*. 2021;50(12):6734-6789.
115. Le Comte A, Reynier Y, Vincens C, Leys C, Azais P. First prototypes of hybrid potassium-ion capacitor (KIC): an innovative, cost-effective energy storage technology for transportation applications. *J Power Sources*. 2017;363:34-43.

116. Kaliyappan K, Chen Z. Atomic-scale manipulation of electrode surface to construct extremely stable high-performance sodium ion capacitor. *Nano Energy*. 2018;48:107-116.
117. Lim E, Jo C, Kim MS, et al. High-performance sodium-ion hybrid supercapacitor based on Nb_2O_5@carbon core-shell nanoparticles and reduced graphene oxide nanocomposites. *Adv Funct Mater*. 2016;26(21):3711-3719.
118. Dong S, Li Z, Xing Z, Wu X, Ji X, Zhang X. Novel potassium-ion hybrid capacitor based on an anode of $K_2Ti_6O_{13}$ microscaffolds. *ACS Appl Mater Interfaces*. 2018;10(18):15542-15547.
119. Zhang Z, Li M, Gao Y, et al. Fast potassium storage in hierarchical $Ca_{0.5}Ti_2(PO_4)_3$@C microspheres enabling high-performance potassium-ion capacitors. *Adv Funct Mater*. 2018;28(36):1802684.
120. Luan Y, Hu R, Fang Y, et al. Nitrogen and phosphorus dual-doped multilayer graphene as universal anode for full carbon-based lithium and potassium ion capacitors. *Nano-Micro Lett*. 2019;11(1):30.
121. Fan L, Lin K, Wang J, Ma R, Lu B. A nonaqueous potassium-based battery-supercapacitor hybrid device. *Adv Mater*. 2018;30(20):1800804.
122. Zhou L, Zhang M, Wang Y, et al. Cubic Prussian blue crystals from a facile one-step synthesis as positive electrode material for superior potassium-ion capacitors. *Electrochim Acta*. 2017;232:106-113.
123. Le Z, Liu F, Nie P, et al. Pseudocapacitive sodium storage in mesoporous single-crystal-like TiO_2-graphene nanocomposite enables high-performance sodium-ion capacitors. *ACS Nano*. 2017;11(3):2952-2960.
124. Chen Z, Augustyn V, Jia X, Xiao Q, Dunn B, Lu Y. High-performance sodium-ion pseudocapacitors based on hierarchically porous nanowire composites. *ACS Nano*. 2012;6(5):4319-4327.

SUPPORTING INFORMATION

Additional supporting information can be found online in the Supporting Information section at the end of this article.

How to cite this article: Cheng G, Zhang W, Wang W, et al. Sulfur and nitrogen codoped cyanoethyl cellulose-derived carbon with superior gravimetric and volumetric capacity for potassium ion storage. *Carbon Energy*. 2022;1-16. doi:10.1002/cey2.233